Journal of Biomedical Optics

SPIEDigitalLibrary.org/jbo

Vital-dye-enhanced multimodal imaging of neoplastic progression in a mouse model of oral carcinogenesis

Anne Hellebust
Kelsey Rosbach
Jessica Keren Wu
Jennifer Nguyen
Ann Gillenwater
Nadarajah Vigneswaran
Rebecca Richards-Kortum

SPIE

Vital-dye-enhanced multimodal imaging of neoplastic progression in a mouse model of oral carcinogenesis

Anne Hellebust,[a] Kelsey Rosbach,[a] Jessica Keren Wu,[b] Jennifer Nguyen,[b] Ann Gillenwater,[c] Nadarajah Vigneswaran,[b] and Rebecca Richards-Kortum[a,*]
[a]Rice University, Department of Bioengineering, 6100 Main Street, Houston, MS-142, Texas 77005
[b]University of Texas Dental Branch at Houston, Department of Diagnostic and Biomedical Sciences, 7500 Cambridge Street, Houston, Texas 77054
[c]University of Texas, M.D. Anderson Cancer Center, Department of Head and Neck Surgery, 1515 Holcombe Boulevard, Unit 441, Houston, Texas 77030

Abstract. In this longitudinal study, a mouse model of 4-nitroquinoline 1-oxide chemically induced tongue carcinogenesis was used to assess the ability of optical imaging with exogenous and endogenous contrast to detect neoplastic lesions in a heterogeneous mucosal surface. Widefield autofluorescence and fluorescence images of intact 2-NBDG-stained and proflavine-stained tissues were acquired at multiple time points in the carcinogenesis process. Confocal fluorescence images of transverse fresh tissue slices from the same specimens were acquired to investigate how changes in tissue microarchitecture affect widefield fluorescence images of intact tissue. Widefield images were analyzed to develop and evaluate an algorithm to delineate areas of dysplasia and cancer. A classification algorithm for the presence of neoplasia based on the mean fluorescence intensity of 2-NBDG staining and the standard deviation of the fluorescence intensity of proflavine staining was found to separate moderate dysplasia, severe dysplasia, and cancer from non-neoplastic regions of interest with 91% sensitivity and specificity. Results suggest this combination of noninvasive optical imaging modalities can be used *in vivo* to discriminate non-neoplastic from neoplastic tissue in this model with the potential to translate this technology to the clinic. *© The Authors. Published by SPIE under a Creative Commons Attribution 3.0 Unported License. Distribution or reproduction of this work in whole or in part requires full attribution of the original publication, including its DOI.* [DOI: 10.1117/1.JBO.18.12.126017]

Keywords: optical imaging; fluorescence; microscopy; carcinogenesis; mouse cancer model; contrast agents.

Paper 130541R received Jul. 30, 2013; revised manuscript received Oct. 24, 2013; accepted for publication Nov. 20, 2013; published online Dec. 20, 2013.

1 Introduction

Early cancer detection is critical to reducing the mortality and morbidity of oral cancers.[1] Currently, histopathological examination of an incisional biopsy after white light examination is the gold standard for diagnosis of oral cancer and its precursor lesions.[2] However, biopsy is an invasive, time-consuming, and expensive procedure that may not be representative of larger lesions.[3] Optical imaging has the potential to noninvasively identify and monitor neoplastic changes in tissue using a combination of endogenous and exogenous tissue contrast. Endogenous optical contrast can provide information about changes in the tissue architecture and cellular metabolism for detection of neoplastic lesions.[4,5] Topically applied, molecular specific contrast agents can be used to visualize changes in biomarker expression to further increase image contrast between neoplastic and non-neoplastic tissue to facilitate detection at the earliest possible stages.

Endogenous tissue fluorescence (autofluorescence) is used as a noninvasive diagnostic aid to detect preinvasive and clinically occult malignant lesions of oral mucosa.[6] Currently, two U.S. Food and Drug Administration (FDA)-approved autofluorescence-based oral mucosal devices (i.e., VELscope and Identafi™ 3000) are widely used by general dental practitioners for early detection of potentially malignant oral lesions. These devices allow for identification of oral mucosal preneoplastic and neoplastic lesions from normal mucosal with high sensitivity.[7,8] However, these instruments are less reliable in discriminating benign inflammatory lesions from potentially malignant lesions as well as lesions with increased risk of progression.[9–12]

The addition of topically applied, targeted optical contrast agents has the potential to improve the diagnostic specificity of noninvasive widefield imaging devices by mapping the expression of multiple biomarkers across a heterogeneous area of tissue and tracking changes over time.[4,5,13] Changes in cell metabolism and nuclear morphology are two accepted and well-documented biomarkers of carcinogenesis.[14,15] (2-(N-(7-Nitrobenz-2-oxa-1,3-diazol-4-yl)Amino)-2-Deoxyglucose) (2-NBDG) is a fluorescent deoxyglucose molecule that enters metabolically active cells via glucose transporters; it is phosphorylated upon transport and entrapped inside individual cells.[16,17] 2-NBDG is a reporter of glycolysis, following the same pathway of D-glucose.[18] Thus, fluorescence of cells labeled with 2-NBDG provides a marker of metabolic activity. A variety of tumors show increased 2-NBDG uptake.[19–21] Similarly, nuclear enlargement, nuclear pleomorphism, and increased nuclear density are well-defined biomarkers of neoplasia. Proflavine, a fluorescent dye that binds to DNA, allows for visualization of nuclear morphology.[22] Cell nuclei are stained specifically yielding a high signal-to-noise ratio in nonkeratinized tissue, allowing for nuclear-to-cytoplasmic ratio calculations.[23,24] In keratinized tissue, keratin is also associated with proflavine staining. Although proflavine is not yet approved by FDA for internal use in the oral cavity, it has a long history of safe clinical use as a topical antiseptic agent.[25]

*Address all correspondence to: Rebecca Richards-Kortum, E-mail: rkortum@rice.edu

Cancers of the oral cavity and pharynx occur in distinct anatomic locations; the most common site of occurrence is the tongue, which accounts for 28% of these lesions.[1] The most significant histologic difference between anatomic sites within the oral cavity is the presence or absence of keratin. Tongue cancer is highly representative of neoplastic lesions that arise in keratinized oral sites. For this study, an animal model that closely simulates the clinical and biological aspects of human tongue cancer development and progression was used to explore endogenous and exogenous contrast throughout the dysplasia-carcinoma sequence. Mice fed with the DNA adduct forming 4-nitroquinoline 1-oxide (4NQO) in their drinking water exhibit DNA damage similar to that of tobacco carcinogens, and the resulting oral neoplastic transformation is histologically similar to that seen in oral cancer patients.[26,27] This murine model provides an opportunity to optimize and validate noninvasive optical imaging techniques with the potential for long-term *in vivo* imaging studies to track progression over time.

The goal of this study was to assess the ability of exogenous and endogenous optical contrast for detection of progressive neoplastic lesions, especially across a heterogeneous mucosal surface. To accomplish this goal, widefield fluorescence images of unstained, 2-NBDG-stained, and proflavine-stained tissue were acquired at multiple time points in the carcinogenesis process; digital images were analyzed to develop and evaluate an algorithm to delineate areas of neoplasia. High-resolution confocal images of fresh transverse slices were obtained to improve the understanding of how changes in tissue microarchitecture affect widefield fluorescence images of intact tissue.

2 Materials and Methods

2.1 *Mouse Tongue Carcinogenesis Model*

Six-week-old female CBA/J mice were purchased from Jackson Laboratories (Bar Harbor, Maine). Animals were treated with 4NQO at 100 μg/mL in their drinking water for 16 weeks to induce epithelial carcinogenesis. In this murine model, over half of the specimens developed dysplasia by 12 weeks and squamous cell carcinoma (SCC) by 24 weeks.[28] Animals were euthanized at various time points during the treatment process (Table 1). Following sacrifice, the tongue was removed for imaging experiments as described below. All animal experiments were reviewed and approved by the Institutional Animal Care and Use Committee of the University of Texas School of Dentistry at Houston.

2.2 *Widefield Imaging*

White light and fluorescence widefield images were captured with a multispectral digital microscope (MDM), which is described in detail elsewhere.[29] Briefly, the system is an optical microscope that has been modified to capture digital white light images and fluorescence images at multiple excitation wavelengths. The MDM captures images with a field of view of $\sim 3 \times 2$ cm. In this study, the MDM was used to capture autofluorescence images at 405 nm excitation with a 430 nm long-pass emission filter, as well as fluorescence images following topical application of two fluorescent contrast agents. Fluorescence images following topical staining with 2-NBDG were obtained with an excitation of 450 nm and a 550 nm long-pass emission filter; following topical staining with proflavine, images were obtained with an excitation of 450 nm using a 490 nm long-pass filter. The gain and exposure time were kept constant for each modality. Fluorescent standards and a frosted quartz disk were imaged during each imaging session/time point as positive and negative controls. Of particular importance, the green and blue fluorescent slides maintained a mean fluorescence intensity within $\pm 7\%$ over the course of the study, and the negative control showed minimal fluorescence above the background.

After each specimen was harvested, white light and autofluorescence images of the resected tissue were obtained. Specimens were then incubated in a 160 μM solution of 2-NBDG (Invitrogen, Carlsbad, California) in 1X phosphate-buffered saline (PBS) for 20 min at 37°C. Uptake of this fluorescent deoxyglucose derivative is associated with increased metabolic activity.[16,17] Specimens were washed once with PBS and then fluorescence images were obtained using the appropriate filters for 2-NBDG imaging. The specimen was next incubated in a 0.01% w/v solution of proflavine (Sigma Aldrich, St. Louis, Missouri) in 1X PBS for 2 min at room temperature. Specimens were washed once with PBS and then fluorescence images were obtained using the appropriate filters for proflavine imaging. The fluorescence signal from proflavine staining is much brighter than that of 2-NBDG, allowing for imaging of proflavine-stained tissue after 2-NBDG staining. Table 1 shows the number of samples imaged with each modality at each time point; white light and autofluorescence images were obtained from all specimens, but some specimens were not stained with 2-NBDG and proflavine but were reserved for confocal imaging as described below.

2.3 *Confocal Microscopy*

Widefield fluorescence images characterize variations in tissue autofluorescence and uptake of the contrast agent across the epithelial surface. To qualitatively assess the distribution of fluorescence throughout the epithelium and stroma, confocal fluorescence images were collected from transverse fresh tissue slices of some specimens. Resected specimens were stored in iced phenol-free Dulbecco's modified Eagle's medium (Sigma-Aldrich, St. Louis, Missouri) until slicing. Approximately 300-μm-thick transverse tissue slices were prepared using a Krumdieck tissue slicer (Alabama Research and Development, Munford, Alabama). Slices were prepared from both unstained specimens and stained specimens, but were not fixed prior to imaging. Confocal images were acquired using a Zeiss LSM 5 Live confocal microscope (Carl Zeiss, Inc., Thornwood, New York) within 12 h of specimen collection. Images were obtained using a 20× objective (NA 0.8). The focal plane was located between 15 and 25 microns below the surface of the tissue slice. Autofluorescence images were obtained at both 405 and 488 nm excitation, and collected

Table 1 Number of specimens imaged for each modality by time point.

Time (weeks)	0 (control)	11	14	21	26	29
Autofluorescence	9	3	4	2	3	5
2-NBDG	6	2	2	1	2	4
Proflavine	4	1	2	1	1	3

with 420 and 505 nm long-pass filters, respectively. Images from proflavine-stained specimens were obtained at 488 nm excitation using a 505 nm long-pass filter. All images were taken with the same detector settings for each modality. Confocal images were not obtained from specimens stained with 2-NBDG due to photobleaching. 2-NBDG fluorescence is more prone to photobleaching than is autofluorescence or proflavine.

2.4 *Pathology Maps*

Following all imaging experiments, tissue specimens were fixed in 10% formalin and returned to the Pathology Department of University of Texas School of Dentistry at Houston for hematoxylin and eosin (H&E) staining. To facilitate the comparison of widefield images to a histologic reference standard, a two-dimensional color-coded pathology map was created for each specimen. Histological sections were obtained for each section cut by the Krumdieck tissue slicer. The H&E slide from each section was reviewed by an oral pathologist (N.V.), who segmented the section into regions of normal/benign epithelium, mild, moderate, and severe dysplasia, and SCC using published criteria for grading oral epithelial dysplasia.[30] A color-coded two-dimensional pathology map was then created by registering the adjacent segmented sections; this map could then be superimposed on top of white light or fluorescence images from the same sample.

2.5 *Image Analysis*

Confocal fluorescence images were qualitatively analyzed to identify key morphologic features associated with autofluorescence and proflavine uptake. These features correspond to those present in H&E-stained histology, including changes in keratin structure, nuclear crowding, and nuclear enlargement. Images of the epithelium were divided into three layers that are routinely used for histopathologic assessment to qualitatively describe spatial patterns in autofluorescence and proflavine staining throughout neoplastic progression.

The data used for quantitative image analysis were compiled from 12 of the 25 total specimens, which were selected because widefield images of autofluorescence, 2-NBDG, and proflavine were obtained for each of these specimens. Images from these three modalities were aligned with a built-in image registration algorithm and analyzed using MATLAB® software (The MathWorks, Natick, Massachusetts). A 25×25 pixel grid was used to divide images into regions of interest (ROIs). Between 83 and 125 ROIs were created per specimen. The mean of the fluorescence intensity and the kurtosis, entropy, skewness, and standard deviation of the pixel histogram of fluorescence intensity were calculated for each ROI in each of the three imaging modalities. Each ROI was assigned a pathology read based on the corresponding pathology maps. ROIs without a corresponding pathology read due to missing epithelium in the histologic section were excluded from further analysis.

A two-class linear discriminant analysis-based classifier was developed to discriminate non-neoplastic from neoplastic ROIs based on quantitative feature values. The data set was split into a training and test set. The training and test groups were created by dividing the 12 specimens into two groups based on duration of carcinogen application to ensure both early and late time points were included into each set. All of the ROIs from an individual specimen were designated to either the training or test set to ensure all of the ROIs for an individual specimen were only in one of the two sets. The data sets contain a similar number of ROIs per diagnostic category (Table 2). For training and testing, moderate dysplasia, severe dysplasia, and SCC were grouped together as neoplastic samples. ROIs with mild dysplasia were excluded from the algorithm development. The algorithm generates a posterior probability that an ROI is neoplastic based on image features calculated from each imaging modality; samples with a posterior-probability exceeding the 0.39 threshold were classified as neoplastic. Performance measures, such as the area under the receiver operating curve (AUC), sensitivity, and specificity at the Q-point, were calculated for each of the individual image features using the pathology read as the gold standard. The two features with the best combined performance in distinguishing neoplastic tissue from non-neoplastic tissue were selected based on the AUC. The algorithm was then used to classify the held-out samples with a histologic diagnosis of mild dysplasia.

3 Results

3.1 *Mouse Tongue Carcinogenesis Model*

A total of 25 mice were examined in this study. Nine animals served as controls and were not exposed to the carcinogen; the remaining 16 animals were exposed to the carcinogen and sacrificed at different time points (Table 1). The number of specimens imaged differed between imaging modalities because some specimens were saved for confocal imaging. Specimens

Table 2 Number of regions of interest (ROIs) and performance of the classification algorithm for the training and test groups by histologic diagnosis.

	Training group		Test group		No assignment	
Histologic diagnosis	Number of ROIs	Classified non-neoplastic (%)	Number of ROIs	Classified non-neoplasic (%)	Number of ROIs	Classified non-neoplastic (%)
Normal	237	82	250	91		
Mild dysplasia					199	42
Moderate dysplasia	130	29	130	11		
Severe dysplasia	24	8	30	0		
Squamous cell carcinoma	5	20	5	0		

destined for autofluorescence confocal imaging were not topically stained with 2-NBDG or proflavine to allow the autofluorescence signal to be imaged. Similarly, specimens destined for 2-NBDG confocal imaging were not topically stained with proflavine. In this model, dysplasia begins four weeks after exposure, and half of the specimens develop dysplasia by week 12.[28] SCC is seen 18 weeks postexposure, and half of the specimens develop SCC by 24 weeks, but the carcinogenesis process is multifocal with multiple lesions forming at different sites on the tongues.

3.2 *Widefield Imaging*

Widefield white light, autofluorescence, and fluorescence images poststaining with 2-NBDG and proflavine from the course of the study are shown in Fig. 1. An increase in the blue channel of the autofluorescence images is seen at weeks 11 and 14. With increased carcinogen exposure, blue autofluorescence intensity decreases, but is never completely lost, as seen in images acquired at weeks 21 and 29. Punctate areas of increased autofluorescence in the red channel are visible after the 14-week time point. Areas of increased red autofluorescence are often found near ulcerated regions of tissue and have been associated with oral bacteria.[31] For comparison, a control specimen that was not exposed to the carcinogen is shown in the column on the left, which shows minimal autofluorescence signal; this remained essentially constant at all time points (data not shown).

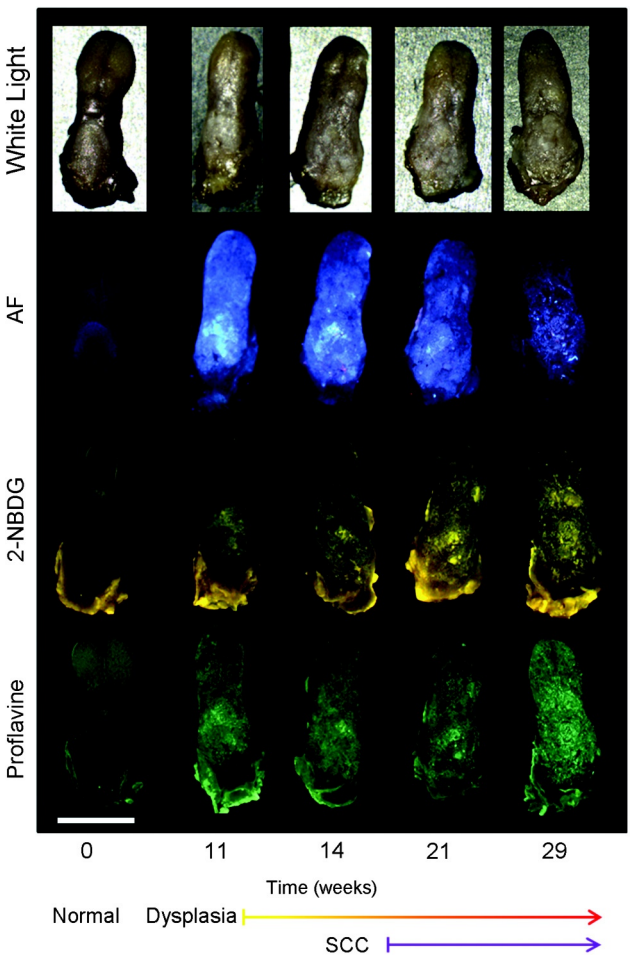

Fig. 1 *Ex vivo* widefield imaging of mouse tongues. White light and autofluorescence images of unstained mouse tongues are shown in the top two rows, respectively. Fluorescence images acquired after staining the specimens with 2-NBDG and proflavine are shown below. A control specimen that was not exposed to the carcinogen is shown in the left column. Specimens at 11, 14, 21, and 29 weeks after initial carcinogen exposure are shown from left to right. Dysplasia begins at 4 weeks postexposure with over half of the specimens developing dysplasia by 12 weeks. Squamous cell carcinoma (SCC) is seen 18 weeks postexposure with over half of the specimens developing SCC by 24 weeks.[28] Scale bar is 5 mm.

Focal areas of increased fluorescence intensity with 2-NBDG labeling are seen beginning at week 11 and increase over time throughout the study. The total area of increased fluorescence intensity per specimen also rises over time. High fluorescence intensity near the base of the tongue is due to nonspecific uptake of the cut edge. Removal of excess dye from the cut edge with exposed muscular tissue is difficult, leading to higher background; similar spreading of India ink occurs in muscular tissue for pathology. However, cut edges and ulcerations are detectable under white light examination, allowing these areas to be excluded from the analysis of fluorescence images.

Proflavine staining reveals changes in surface texture as a function of time. The fluorescence image of a normal specimen labeled with proflavine shows a regular periodic pattern. This pattern is disrupted beginning at week 11; there is a progressive increase in bright, punctate spots of proflavine staining with time across the course of the study. The number of focal areas of increased proflavine fluorescence per specimen rises over time with carcinogen exposure.

3.3 *Confocal Microscopy*

Fluorescence confocal images of fresh transverse tissue slices were collected to improve the understanding of how changes at the cellular level affect widefield fluorescence images of intact tissue. Figure 2 shows autofluorescence confocal images of epithelial cross-sections. The blue channel utilized 405 nm excitation, the same as that used in widefield imaging. The green channel illustrates epithelial cell size and morphology. Images were collected as two separate channels and superimposed in Fig. 2. Corresponding H&E images from the same tissue slices are shown below [Figs. 2(f) to 2(j)]. The images are grouped by pathology grade ranging from normal [Figs. 2(a) and 2(f)], through multiple stages of dysplasia [Figs. 2(b) to 2(d) and 2(g) to 2(i)] and SCC [Figs. 2(e) and 2(j)]. The superficial layer of normal epithelium shows a bright layer of blue autofluorescence corresponding to superficial keratin. The pattern of autofluorescence follows the periodic filiform papillae structure of the underlying epithelium. The superficial keratin autofluorescence increases for the sample with mild dysplasia [white arrow, Fig. 2(b)]; this signal corresponds to the hyperkeratosis [black arrow, Fig. 2(g)] present in the H&E-stained section. In general, the autofluorescence from the keratin layer decreases as the thickness of keratin decreases with progression of the disease. However, these specimens contain keratin of highly variable thickness at all stages of disease. These findings are also seen in the corresponding H&E-stained sections.

Beneath the superficial keratin, normal epithelial cells show weak green autofluorescence, which is strongest in the basal portion of the epithelium [Fig. 2(a)]. With progression to mild dysplasia, the cellular fluorescence encompasses the lower third of the epithelium [Fig. 2(b)]. Cellular fluorescence signal is observed in the lower two thirds of the epithelium in the

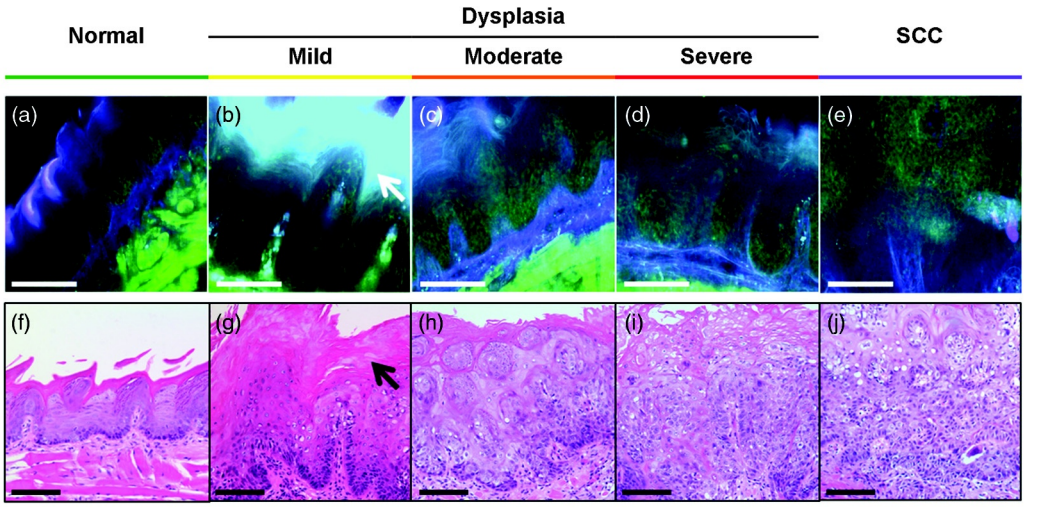

	Normal	Mild	Moderate	Severe	SCC
Keratin	• Moderate intensity • Regular, periodic pattern	• High intensity • Loss of periodic pattern	• Moderate intensity • Loss of periodic pattern	• Low intensity • Loss of keratin	• Low intensity • Loss of keratin
Epithelial Cells	• Low intensity • Basal epithelium	• Low intensity • Lower third of the epithelium	• Moderate intensity • Two thirds of the epithelium	• Moderate intensity • Full thickness	• Moderate intensity • Throughout
Stromal Collagen	• Weak intensity	• Strong intensity	• Moderate intensity	• Moderate intensity	• Moderate intensity

Fig. 2 High-resolution, cross-sectional images of mouse tongue epithelium corresponding to areas imaged with widefield autofluorescence imaging. Confocal autofluorescence images [(a) to (e)] are matched with H&E-stained histology sections [(f) to (j)] from the same specimen. Images are grouped by pathology grade: normal [(a) and (f)], mild dysplasia [(b) and (g)], moderate dysplasia [(c) and (h)], severe dysplasia [(d) and (i)], and squamous cell carcinoma [(e) and (j)]. Arrows indicate hyperkeratosis. Qualitative features of the confocal autofluorescence images for the keratin, epithelial cell, and stromal collagen layers are listed in the table below the figure. Scale bars are 100 μm.

specimen with moderate dysplasia [Fig. 2(c)]. The epithelial cells in severe dysplasia and cancer exhibit moderately intense fluorescence throughout the epithelium and in cellular regions of the tumor, respectively [Figs. 2(d) and 2(e)].

Proflavine staining highlights cell nuclei [Figs. 3(a) to 3(e)]. In keratinized tissue, the keratin is also stained by proflavine. A regular, periodic keratin pattern is seen in the fluorescence images of normal tissue [Fig. 3(a)]. This periodic pattern is disrupted and ultimately lost with progression from dysplasia to SCC. In normal tissue, strong epithelial cell nuclear staining is seen in the basal portion of the epithelium [Fig. 3(a)]. As expected, cell nuclei become enlarged and crowded with progression to dysplasia and cancer. The proflavine fluorescence signal from cell nuclei encompasses the lower half of the epithelium in mild dysplasia [Fig. 3(b)], the lower two thirds of the epithelium in moderate dysplasia [Fig. 3(c)], and the entire epithelium in severe dysplasia [Fig. 3(d)]. In cancer, enlarged cell nuclei are seen throughout the specimen [Fig. 3(e)]. Proflavine-associated fluorescence in areas of increased keratin is especially prevalent in the mild dysplasia example [Fig. 3(b)]. Corresponding H&E images from the same tissue slices are shown for comparison in Figs. 3(f) to 3(j).

3.4 *Ex Vivo Widefield Image Processing*

Figure 4 shows a representative pathology map for one of the specimens in this study. Images from each modality were registered and a pathology map was created based on a detailed pathology review. The colored regions overlaid on the white light image indicate the pathology read. Qualitative comparison of the fluorescence images and the gold standard pathology map demonstrates that there is greater fluorescence intensity in areas of higher degrees of dysplasia and cancer. For example, the area of tissue marked as cancer (purple) on this specimen shows increased fluorescence intensity in the same region in the autofluorescence as well as the 2-NBDG and proflavine-stained images. Additionally, Fig. 4 emphasizes the multifocal lesions formed in this model and the spatial heterogeneity in the histology across a single tissue specimen.

While 2-NBDG images highlight areas of increased fluorescence intensity, the proflavine images accent the heterogeneity of the surface texture across the tissue. The changes in keratin surface structure with dysplastic progression are highlighted by the widefield proflavine images shown in Fig. 5(a). ROIs corresponding to different pathology diagnoses are shown at higher magnification in Fig. 5(c). The regular, repeated structure of the papilla and surface keratin is visualized in the normal region [Fig. 5(b)]. Progression through dysplasia leads to a disruption of this pattern, which is completely lost with progression to cancer.

3.5 *Linear Discriminant Analysis*

The ROIs were divided into a training set and test set. Table 2 details the number of ROIs by diagnostic category in each set. One hundred ninety-nine ROIs with a diagnosis of mild

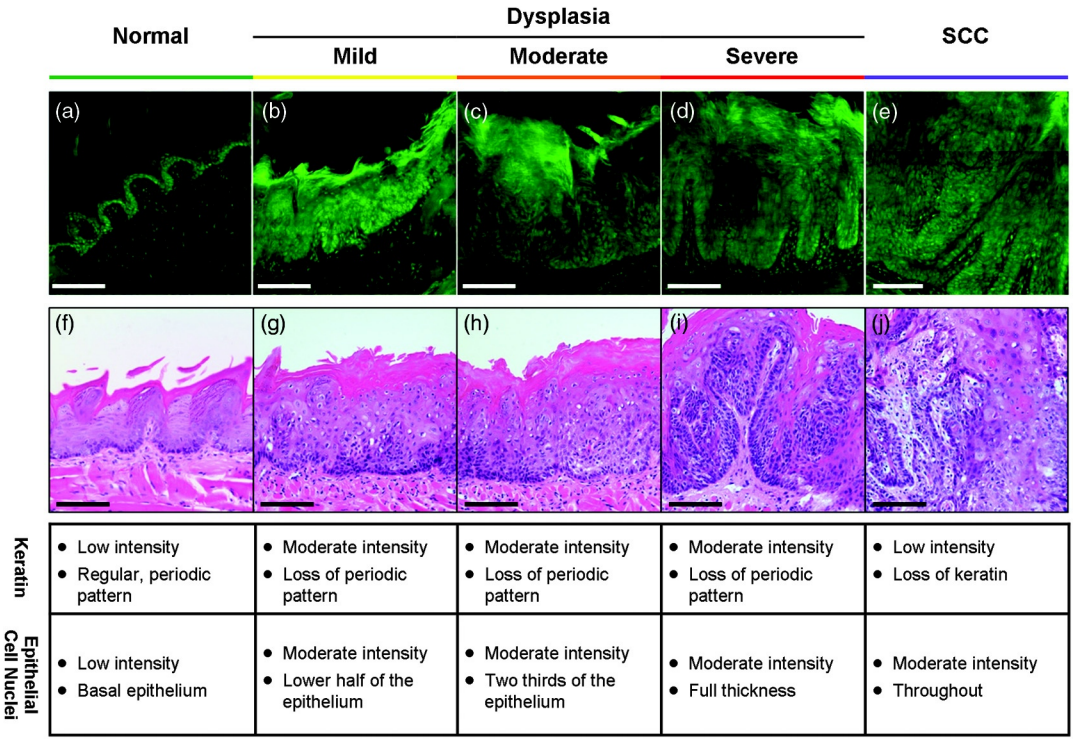

	Normal	Mild Dysplasia	Moderate Dysplasia	Severe Dysplasia	SCC
Keratin	• Low intensity • Regular, periodic pattern	• Moderate intensity • Loss of periodic pattern	• Moderate intensity • Loss of periodic pattern	• Moderate intensity • Loss of periodic pattern	• Low intensity • Loss of keratin
Epithelial Cell Nuclei	• Low intensity • Basal epithelium	• Moderate intensity • Lower half of the epithelium	• Moderate intensity • Two thirds of the epithelium	• Moderate intensity • Full thickness	• Moderate intensity • Throughout

Fig. 3 High-resolution, cross-sectional images of mouse tongue epithelium corresponding to areas imaged with widefield system following proflavine application. Confocal proflavine images [(a) to (e)] and H&E-stained histology sections [(f) to (j)] from the same specimen. Images are grouped by pathology grade: normal [(a) and (f)], mild dysplasia [(b) and (g)], moderate dysplasia [(c and (h)], severe dysplasia [(d and (i)], and squamous cell carcinoma [(e and (j)]. Qualitative features of the confocal proflavine images for the keratin and epithelial cell layers are listed in the table below the figure. Scale bars are 100 μm.

dysplasia were withheld from the initial analysis. The image features in the training set were used to select the two top performing image features and train a classification algorithm to differentiate neoplastic from non-neoplastic ROIs. Proflavine standard deviation and 2-NBDG mean fluorescence intensity were the two top performing features to discriminate neoplastic and non-neoplastic tissue with an area under the receiver operating characteristic curve of 0.96.

A scatter plot of the proflavine standard deviation and 2-NBDG mean fluorescence intensity is shown for the 415 ROIs

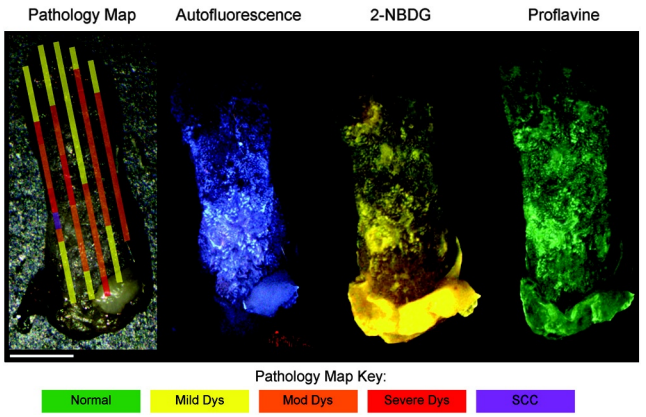

Fig. 4 A representative specimen with the corresponding pathology map. All images were registered in MATLAB® and a pathology map was created based on a pathology review. The color scale on the bottom shows the key for the pathology map. Scale bar is 2.5 mm.

in the test set in Fig. 6(a). In the test group, 89% (116/130), 100% (30/30), and 100% (5/5) of the moderate dysplasias, severe dysplasias, and SCCs were correctly classified as neoplastic, respectively. Of the normal ROIs, 91% (228/250) were correctly classified by the algorithm as non-neoplastic. The algorithm yields a sensitivity and specificity of 91% at the Q-point, the location on the curve with the shortest Euclidean distance to the upper left-hand corner of the plot. Mild dysplasias were excluded from the training algorithm due to the difficulty in accurately making this histological diagnosis and its uncertain clinical potential.[32] When the classifier is applied to ROIs diagnosed histologically as mild dysplasia, 42% (84/199) are classified as non-neoplastic and 58% (115/199) classified as neoplastic. Interestingly, this is similar to recent results reported for the diagnostic accuracy of optical imaging in patient samples.[32] Although intriguing, this does not indicate that these are two distinguishable populations. Figure 6(b) shows a scatter plot of the proflavine standard deviation versus the mean 2-NBDG fluorescence intensity for the samples diagnosed histologically as mild dysplasia.

4 Discussion

In summary, we report the use of a mouse model of chemically induced tongue carcinogenesis to image the progression of precancer to cancer with optical imaging combined with topically applied molecular imaging agents. The combination of vital dyes used in this study, proflavine and 2-NBDG, assesses two potentially relevant biomarkers in oral cancer, nuclear morphology and metabolic activity, respectively. The use of these vital dyes in

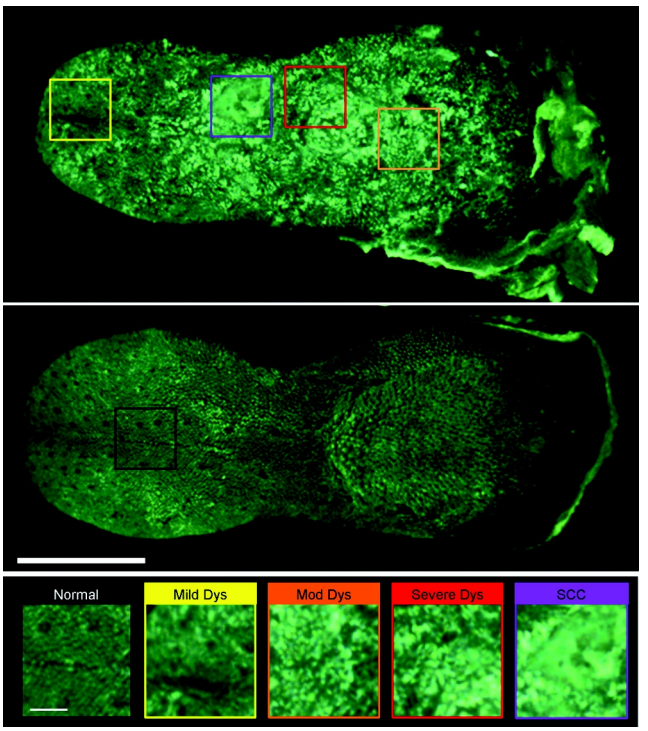

Fig. 5 Changes in keratinized tongue texture versus pathology grade. Structural changes in the keratinized surface are apparent with progression of disease in a carcinogen-exposed proflavine stained specimen (a). A control proflavine stained specimen (b) is shown for comparison. Scale bar is 2.5 mm for widefield images. Enlarged areas of interest corresponding to each of the five diagnostic categories are below (c). Scale bar is 0.5 mm for insets.

combination with autofluorescence imaging allows an area of heterogeneous mucosa to be assessed. Confocal images of fresh transverse tissue slices were used to improve our understanding of the changes depicted in widefield images of the mucosal surface. A classification algorithm separates neoplastic ROIs from normal regions of interest of specimens with an area under the curve of 0.96 when mild dysplasias are excluded from analysis. These results suggest that a combination of optical imaging modalities may be used to discriminate non-neoplastic from neoplastic tissue in this model with the potential to progress to *in vivo* animal studies and ultimately potentially translate these imaging modalities to the clinic.

This 4NQO model is advantageous because all treated animals develop dysplasia and cancer on the keratinized dorsal tongue with histological and molecular similarities to oral cancer progression in patients. 4NQO, a DNA adduct forming agent causing DNA damage, leads to the progression of dysplasia mimicking the damage induced by tobacco smoke in humans, which is an important risk factor for development of oral cancer.[33] This type of model allows the study of precancerous lesions, which is not possible with orthotopic and xenotopic tumors, which require experienced personnel to initiate the tumor along with inducing trauma to the area of implantation. Increased uptake of 2-NBDG is present in regions with advanced lesions as seen in resected human neoplastic tissue, which is indicative of increased metabolic activity.[13,19,20] Additionally, the classification algorithm categorizes normal and dysplastic ROIs with a sensitivity and specificity of 91% each with the exception of mild dysplasia.

However, the model varies from humans in a number of important ways. This model only accounts for molecular changes and progression due to a carcinogen associated with smoking tobacco. This pathway is only one of several leading to oral carcinogenesis; this difference in the molecular basis of individual tumors is responsible for the differences in growth characteristics and response to therapy.[34] Additionally, the heterogeneity of clinical lesions makes finding a single animal model to simulate all types of oral cancer difficult. The thick keratin layer of the dorsal tongue of a mouse is not representative of normal human oral mucosa. This thick keratinized tissue may serve as a model that allows us to study a high-risk form of oral precancer known as proliferative verrucous leukoplakia that is characterized by the development of multiple thick keratotic plaques with roughened surface keratin projections as seen in this model.[35] However, in future studies, the ventral tongue may be imaged in parallel to serve as a nonkeratinized site in the same specimen. The ability to image keratinized and nonkeratinized sites is important due to the differences in the optical

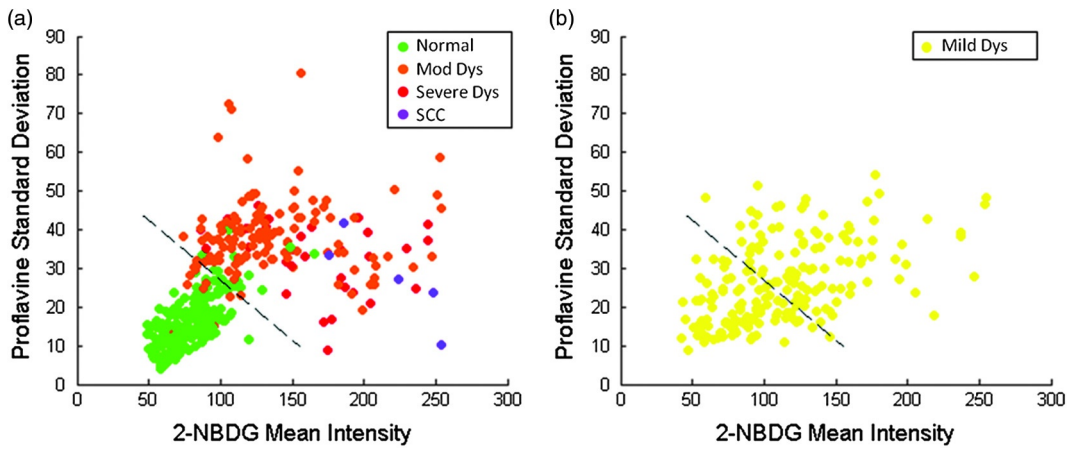

Fig. 6 Classification of ROIs using proflavine standard deviation and 2-NBDG mean fluorescence intensity. Dashed lines represent the linear threshold values to discriminate normal sites from moderate/severe dysplasia or cancer. Plot of wide-field values of proflavine standard deviation and 2-NBDG mean fluorescence intensity for test regions of interest (ROIs) with a pathology diagnosis of normal, moderate dysplasia, severe dysplasia, and squamous cell carcinoma (a). Plot of values for test set ROIs with a pathology diagnosis of mild dysplasia (b). The color scale in upper right corner shows the histology key.

properties and vital dye penetration depths of the two types of tissues.[36] The thin stroma under the epithelium is not similar to the thicker, strongly fluorescent underlying stroma of humans, making widefield autofluorescence imaging not clinically representative. Benign and neoplastic lesions typically observed in the clinic are mixed with varying degrees of inflammation, but this model largely lacks an inflammation component.

One challenge of this study is the highly variable keratin thickness and therefore extremely heterogeneous keratin fluorescence across the surface of these specimens at all stages of disease. The keratin, epithelial, and stromal layers all contribute to the widefield fluorescence images. Increased keratin thickness across a lesion can contribute significantly to the widefield autofluorescence signal, whereas the autofluorescence signal in areas with thin keratin is determined primarily by the epithelial fluorescence. Dramatic changes in keratin thickness can occur over a very short spatial distance (<1 mm). Additionally, spatial registration of widefield images with histopathology was another challenge of this study. Although every effort was made to match pathology maps with the widefield tissue, there is some inherent registration error due to the small size of these specimens.

The confocal images of fresh transverse tissue slices give us qualitative insight as to how changes in the microarchitecture of the tissue influence the corresponding widefield images. The cross-sectional view allows us to localize where in the keratin layer, epithelium, or stroma the fluorescent signal arises. In patients, autofluorescence properties of healthy and diseased oral mucosa are largely dependent on the fluorescent crosslinks of the underlying structural fibers in the stoma such as collagen.[12] However, the thin stroma of the mouse tongue reduces the contribution of stromal autofluorescence to the overall autofluorescence observed in widefield images, making this model different from the clinical presentation of lesions in patients. Although interesting to examine the endogenous signal arising from the epithelium and keratin layers, these differences could be difficult to detect in the presence of the background of strong collagen fluorescence seen clinically. For this reason, image analysis focused on the fluorescent contrast agents targeting the epithelium, which has similar structure to that seen in normal and neoplastic patient samples.

However, a qualitative assessment of the confocal autofluorescence images yields insight into the epithelial changes that occur. The bright blue autofluorescence in the superficial, keratinized epithelial layer of the tissue is the dominant source of autofluorescence in normal and early-stage dysplasias, which is lost at later stages of disease leading to a decrease of fluorescence intensity in tissue at later time points. Changes in keratin structure are observed in both autofluorescence and proflavine confocal imaging. However, these specimens contain keratin of highly variable thickness at all stages of disease. The confocal images highlight change in structure and degradation of keratin with the progression of disease, which corresponds to the change in the standard deviation of proflavine staining seen in widefield imaging used in the classification algorithm. When proflavine staining is spatially uniform, the local standard deviation is low. In this study, a periodic spatial pattern of proflavine staining is associated with an intermediate local standard deviation. As neoplasia progresses, we observed heterogeneous proflavine staining without periodicity associated with a large local standard deviation.

Mild dysplasia is clinically challenging because it can represent the initial stage in the progression toward precancer or it can appear as a transient reaction to inflammation, trauma, or allergy.[37] While a large range of values have been reported, the rate of malignant transformation of mild dysplasia is estimated at <5%.[38] Due to this low rate of malignant transformation, there is no established clinical standard of care for patients with mild dysplasia and management consists of long-term clinical follow-up. To further complicate mild dysplasia diagnosis, intraobserver and interobserver variability of grading of mild dysplasia is high.[39] A biomarker to identify those mild dysplastic lesions that are most likely to progress would be valuable to clinicians. Further study is needed to assess whether these optical measurements can be used to identify these mild dysplastic lesions that are most likely to progress.

The ability to evaluate the progression of disease in this model *in vivo* over time is desirable to track and improve understanding of the changes in optical properties associated with progression. A modified protocol for this model would allow us to track and attempt to predict if mild dysplasia will progress to a higher degree of dysplasia or revert to a benign lesion. These studies would explore the link between data from optical measurements and biomarker expression of oral carcinogenesis if combined with immunohistochemistry for proposed biomarkers of progression. Pierce et al. investigated if specific biomarkers correlated with optical imaging to predict progression of cancer.[32] Whether the same biomarkers (Ki-67, p63, PHH3) may be used for mice remains to be tested. Additionally, keratinized surfaces have proven to be an obstacle for optical imaging of the mucosal surface due to the bright autofluorescence signal from these lesions and the masking of enlarged and pleomorphic nuclei. Future work to look into the changes in the structure of keratin that correspond to neoplastic progression would improve our understanding of the relationship between keratin and the underlying neoplastic cells.

The clinical implications of this study include the ability to improve early detection through noninvasive imaging techniques. This model allows us to look at set time points and identify correlations between multimodal imaging and pathology. This study was performed *ex vivo* as a pilot study to evaluate the usefulness of this model with these contrast agents. The next step is to use these contrast agents *in vivo* over multiple time points to monitor disease progression. Additionally, the model allows researchers to investigate markers that increase the risk of progression. If a relationship between *in vivo* optical measurements and biomarker expression for mild dysplasia is found, it could determine the risk of progression in lesions with mild dysplasia.

Acknowledgments

This work is supported through the National Cancer Institute through Bioengineering Research Partnership Grant No. RO1 CA103830-05, National Institute of Dental and Craniofacial Research Grant No. R21 DE019956, Cancer Prevention & Research Institute of Texas under Grant No. RP100932, and National Science Foundation Graduate Research Fellowship under Grant No. 0940902.

References

1. N. Howlader et al., "SEER cancer statistics review, 1975-2009 (Vintage 2009 populations)," http://seer.cancer.gov/csr/1975_2009_pops09/ (22 May 2013).

2. J. S. Leston and P. D. Dios, "Diagnostic clinical aids in oral cancer," *Oral Oncol.* **46**(6), 418–422 (2010).
3. P. Holmstrup et al., "Oral premalignant lesions: is a biopsy reliable?," *J. Oral Pathol. Med.* **36**(5), 262–266 (2007).
4. A. Hellebust and R. Richards-Kortum, "Advances in molecular imaging: targeted optical contrast agents for cancer diagnostics," *Nanomedicine* **7**(3), 429–445 (2012).
5. R. Weissleder and M. J. Pittet, "Imaging in the era of molecular oncology," *Nature* **452**(7187), 580–589 (2008).
6. N. Bedard et al., "Emerging roles for multimodal optical imaging in early cancer detection: a global challenge," *Technol. Cancer Res. Treat.* **9**(2), 211–217 (2010).
7. D. C. G. De Veld et al., "The status of in vivo autofluorescence spectroscopy and imaging for oral oncology," *Oral Oncol.* **41**(2), 117–131 (2005).
8. D. Roblyer et al., "Objective detection and delineation of oral neoplasia using autofluorescence imaging," *Cancer Prev. Res.* **2**(5), 423–431 (2009).
9. J. E. Bouquot, P. Suarez, and N. Vigneswaran, "Oral precancer and early cancer detection in the dental office—review of new technologies," *J. Implant Adv. Clin. Dent.* **2**(3), 47–63 (2010).
10. C. F. Poh et al., "Tracing the "at-risk" oral mucosa field with autofluorescence: steps toward clinical impact," *Cancer Prev. Res.* **2**(5), 401–404 (2009).
11. M. Huber, "Assessment of the VELscope as an adjunctive examination tool," *Tex. Dent. J.* **126**(6), 528–535 (2009).
12. I. Pavlova et al., "Understanding the biological basis of autofluorescence imaging for oral cancer detection: high-resolution fluorescence microscopy in viable tissue," *Clin. Cancer Res.* **14**(8), 2396–2404 (2008).
13. K. J. Rosbach et al., "Optical molecular imaging of multiple biomarkers of epithelial neoplasia: epidermal growth factor receptor expression and metabolic activity in oral mucosa," *Transl. Oncol.* **5**(3), 160–171 (2012).
14. D. Zink, A. H. Fischer, and J. A. Nickerson, "Nuclear structure in cancer cells," *Nat. Rev. Cancer* **4**(9), 677–687 (2004).
15. J. R. Cantor and D. M. Sabatini, "Cancer cell metabolism: one hallmark, many faces," *Cancer Discovery* **2**(10), 881–898 (2012).
16. P. G. Lloyd, C. D. Hardin, and M. Sturek, "Examining glucose transport in single vascular smooth muscle cells with a fluorescent glucose analog," *Physiol. Res.* **48**(6), 401–410 (1999).
17. K. Yoshioka et al., "Intracellular fate of 2-NBDG, a fluorescent probe for glucose uptake activity, in Escherichia coli cells," *Biosci. Biotechnol. Biochem.* **60**(11), 1899–1901 (1996).
18. K. Yamada et al., "A real-time method of imaging glucose uptake in single, living mammalian cells," *Nat. Protoc.* **2**(3), 753–762 (2007).
19. N. Nitin et al., "Molecular imaging of glucose uptake in oral neoplasia following topical application of fluorescently labeled deoxy-glucose," *Int. J. Cancer* **124**(11), 2634–2642 (2009).
20. R. Langsner et al., "Wide-field imaging of fluorescent deoxy-glucose in ex vivo malignant and normal breast tissue," *Biomed. Opt. Express* **2**(6), 1514–1523 (2011).
21. N. Thekkek, S. Anandasabapathy, and R. Richards-Kortum, "Optical molecular imaging for detection of Barrett's-associated neoplasia," *World J. Gastroenterol.* **17**(1), 53–62 (2011).
22. M. Aslanoglu, "Electrochemical and spectroscopic studies of the interaction of proflavine with DNA," *Anal. Sci.* **22**(3), 439–443 (2006).
23. A. L. Polglase et al., "A fluorescence confocal endomicroscope for in vivo microscopy of the upper- and the lower-GI tract," *Gastrointest. Endosc.* **62**(5), 686–695 (2005).
24. N. Thekkek et al., "Vital-dye enhanced fluorescence imaging of GI mucosa: metaplasia, neoplasia, inflammation," *Gastrointest. Endosc.* **75**(4), 877–887 (2012).
25. M. Wainwright, "Acridine—a neglected antibacterial chromophore," *J. Antimicrob. Chemother.* **47**(1), 1–13 (2001).
26. X. H. Tang et al., "Oral cavity and esophageal carcinogenesis modeled in carcinogen-treated mice," *Clin. Cancer Res.* **10**(1), 301–313 (2004).
27. B. Farahati et al., "Rigid confocal endoscopy for in vivo imaging of experimental oral squamous intra-epithelial lesions," *J. Oral Pathol. Med.* **39**(4), 318–327 (2010).
28. R. Hasina et al., "ABT-510 is an effective chemopreventive agent in the mouse 4-nitroquinoline 1-oxide model of oral carcinogenesis," *Cancer Prev. Res.* **2**(4), 385–393 (2009).
29. D. Roblyer et al., "Multispectral optical imaging device for in vivo detection of oral neoplasia," *J. Biomed. Opt.* **13**(2), 024019 (2008).
30. S. Warnakulasuriya et al., "Oral epithelial dysplasia classification systems: predictive value, utility, weaknesses and scope for improvement," *J. Oral Pathol. Med.* **37**(3), 127–133 (2008).
31. W. Dietel et al., "5-aminolaevulinic acid (ALA) induced formation of different fluorescent porphyrins: a study of the biosynthesis of porphyrins by bacteria of the human digestive tract," *J. Photochem. Photobiol. B-Biol.* **86**(1), 77–86 (2007).
32. M. C. Pierce et al., "Accuracy of in vivo multimodal optical imaging for detection of oral neoplasia," *Cancer Prev. Res.* **5**(6), 801–809 (2012).
33. D. Kanojia and M. M. Vaidya, "4-nitroquinoline-1-oxide induced experimental oral carcinogenesis," *Oral Oncol.* **42**(7), 655–667 (2006).
34. H. K. Williams, "Molecular pathogenesis of oral squamous carcinoma," *J. Clin. Pathol.-Mol. Pathol.* **53**(4), 165–172 (2000).
35. A. Gillenwater et al., "Proliferative verrucous leukoplakia (PVL): recognition and differentiation from conventional leukoplakia and mimics!," *Head Neck* (2013).
36. R. A. Schwarz et al., "Prospective evaluation of a portable depth-sensitive optical spectroscopy device to identify oral neoplasia," *Biomed. Opt. Express* **2**(1), 89–99 (2011).
37. M. P. Rosin et al., "Use of allelic loss to predict malignant risk for low-grade oral epithelial dysplasia," *Clin. Cancer Res.* **6**(2), 357–362 (2000).
38. P. M. Speight, "Update on oral epithelial dysplasia and progression to cancer," *Head Neck Pathol.* **1**(1), 61–66 (2007).
39. D. J. Fischer et al., "Interobserver reliability in the histopathologic diagnosis of oral pre-malignant and malignant lesions," *J. Oral Pathol. Med.* **33**(2), 65–70 (2004).

Biographies of the authors are not available.